Survey of Poynting flux of whistler mode chorus in the outer zone

O. Santolík,[1,2,3] J. S. Pickett,[1] D. A. Gurnett,[1] J. D. Menietti,[1] B. T. Tsurutani,[4] and O. Verkhoglyadova[4]

[1]   We present a survey of whistler mode chorus emissions based on high-telemetry rate data of the Plasma Wave Instrument on board the Polar spacecraft. Using simultaneous measurements of full vectors of the electric field and the magnetic field we calculate the Poynting vectors of chorus, and we parameterize the observations by their $L*$ coordinate. Our new analysis of the angle between the direction of the Poynting vector and the magnetic field line confirms previous results on propagation of the main chorus band away from the equator. Our systematic results also prove the existence of the magnetospherically reflected component of chorus found previously by case studies. We observe weak outer zone waves that propagate toward the equator. These waves can be attributed to a poleward reflected component of equatorial chorus or chorus generated in the dayside pockets of a low magnetic field strength. We analyze the probability distribution of the Poynting flux of chorus, and we find that it shows a "heavy tail" feature that can be modeled by a power law or lognormal model. This result has consequences for theories of chorus generation and for methods of statistical characterization of chorus intensities in the frame of radiation belt modeling. We find that the Poynting flux of dayside chorus increases with $L*$ toward the outer zone at $L* > 6$. We estimate that approximately 1% of the Poynting flux of chorus in the outer zone could be sufficient to accelerate electrons in the outer Van Allen radiation belt on the timescale of days.

1. Introduction

[2]   Chorus consists of whistler mode waves that propagate in the magnetosphere of the Earth and outer planets. It is characterized by discrete wave packets of changing frequencies [*Storey*, 1953; *Pope*, 1963; *Burtis and Helliwell*, 1969] which often occur in two bands around one half of the equatorial electron cyclotron frequency [*Tsurutani and Smith*, 1974]. Chorus is recently being considered as a potentially significant component in the studies of the dynamics of the Van Allen radiation belts [e.g., *Tsurutani et al.*, 2006; *Horne*, 2007; *Shprits et al.*, 2007; *Summers et al.*, 2007; *Trakhtengerts et al.*, 2007; *Omura et al.*, 2007, 2008; *Albert*, 2008; *Kasahara et al.*, 2009; *Hikishima et al.*, 2009]. Chorus is generated by unstable electron populations at typical energies of a few tens of keV. At the same time it is also thought to contribute to acceleration of radiation belt electrons to relativistic energies, transferring thus the energy from the low-energy part of the electron distribution function to the relativistic electrons.

[3]   In the Earth's inner magnetosphere, measurements of the Polar and Cluster spacecraft [*LeDocq et al.*, 1998; *Parrot et al.*, 2003a; *Santolík et al.*, 2003a; *Santolík*, 2008] have shown a positive divergence of the Poynting flux and hence the source of chorus in the vicinity of the geomagnetic equatorial plane. Since chorus is an electromagnetic wave that can propagate from its source region, it can influence large and relatively distant regions of the magnetosphere. Ray tracing studies and spacecraft measurements have shown that it can propagate from its equatorial source to high latitudes and down to the ionosphere [*Chum and Santolík*, 2005; *Santolík et al.*, 2006]. It can also penetrate the plasmapause and contribute to the plasmaspheric hiss emissions [*Chum and Santolík*, 2005; *Santolík et al.*, 2006; *Bortnik et al.*, 2008, 2009; *Santolík and Chum*, 2009] that are responsible for the existence of the slot region between the outer and inner electron radiation belts. Another possibility for propagation of whistler mode chorus has been documented by case studies of *Parrot et al.* [2003b, 2004] using the data of the Cluster spacecraft. Ray tracing analysis supported by observational evidence has shown that

---

[1]Department of Physics and Astronomy, University of Iowa, Iowa City, Iowa, USA.
[2]Permanently at Institute of Atmospheric Physics, Prague, Czech Republic.
[3]Permanently at Faculty of Mathematics and Physics, Charles University, Prague, Czech Republic.
[4]Jet Propulsion Laboratory, Pasadena, California, USA.

chorus can magnetospherically reflect at high latitudes and propagate inward and back to the equator. The power spectral density of these returning waves has been found at least 2 orders of magnitude below the level of the original chorus emission.

[4] The low-latitude equatorial region is not the only possible source of chorus. *Tsurutani and Smith* [1977] proposed that chorus can also originate from the dayside outer zone in the Earth's magnetosphere, where the terrestrial magnetic field is compressed by the solar wind, and where local minima of the magnetic field strength occur. This high-latitude source might be consistent with increasing wave amplitudes as a function of the magnetic latitude found on the dayside by *Horne et al.* [2005]. *Nagano et al.* [1996] and *Menietti et al.* [2009], on the contrary, reported chorus propagating from an equatorial source close to the dayside magnetopause and the cusp region. *Vaivads et al.* [2007] have documented an event where the positive divergence of the Poynting flux is observed at high latitudes. This observation is colocalized with the multipoint measurements of minima of the magnetic field strength close to the dayside cusp region. *Verkhoglyadova et al.* [2009] and *Tsurutani et al.* [2009] investigated the dayside outer zone chorus using the waveform measurements of the Geotail spacecraft. They found similar fine structure of subpackets with a duration of 5 to 10 ms inside the chorus wave packets with rising frequency, as it was documented for the equatorial chorus in its source region [*Santolík et al.*, 2003a]. *Tsurutani et al.* [2009] found cases of Geotail dayside high-intensity chorus that were propagating from high latitudes toward the equator.

[5] Numerous recent statistical studies [*Meredith et al.*, 2001, 2002, 2003a, 2003b, 2009; *Santolík et al.*, 2005; *Pokhotelov et al.*, 2008; *Li et al.*, 2009] have described the distribution of chorus intensity and occurrence rate as a function of the magnetic latitude, magnetic local time, radial distance from the Earth, and/or McIlwain's L coordinate, and parameterized these results by the level of geomagnetic activity. To characterize the intensity of chorus these studies use power spectral densities of the magnetic field fluctuations and/or electric field fluctuations or, alternatively, the derived estimates of their narrow-band amplitudes. The only statistics derived up to now from these data are arithmetic averages. These results can serve as an input to the models of radiation belts.

[6] In this paper, we concentrate on three questions linked to these statistical surveys of chorus. (1) Can we successfully replace the McIlwain's L coordinate by the $L*$ coordinate (generalized L value) [*Roederer*, 1970] to parameterize characteristics of whistler mode chorus for radiation belt models? (2) What are the properties of chorus power spectral densities in terms of probability distributions? (3) What are the characteristics of the Poynting flux and the direction of the Poynting vector of chorus?

[7] This study is based on a data set recorded by the Polar spacecraft in 1996 and 1997 and is closely related to the work of *LeDocq et al.* [1998]. We use measurements of six components of the electric and magnetic fluctuations to determine the power spectral densities of fluctuating magnetic and electric fields of chorus, as well as its Poynting flux and the direction of the Poynting vector. Section 2

introduces our data set and analysis methods. Section 3 presents our results on statistics of power spectral densities of chorus with a focus on the outer zone at $L* \approx 7$, and section 4 describes results of a new analysis of directions of the Poynting vector in this zone. Finally, section 5 contains discussion of results and brief conclusions.

2. Data Set and Analysis Methods

[8] The Polar spacecraft was equipped with comprehensive plasma physics instrumentation, including the plasma wave instrument (PWI) designed to measure wave phenomena in magnetospheric plasmas [*Gurnett et al.*, 1995]. The PWI instrument used several different receivers to process measurements from magnetic field and electric field sensors. We use data acquired by the high-frequency waveform receiver (HFWR). This device recorded waveform snapshots from the full set of three orthogonal magnetic search coil antennas and three-component electric field double-sphere antennas. In the high-resolution mode, these six-component waveforms were captured with a sampling rate of 71.4 kHz and organized in snapshots of 0.445 s separated by gaps of 8.755 s. Available frequencies range from 20 Hz to 25 kHz.

[9] The same data set has been reported by *LeDocq et al.* [1998], who examined the high-resolution HFWR data from 394 orbits of the Polar spacecraft and selected clear examples of chorus recorded during 59 orbits between 1 April 1996 and 15 September 1997. The data predominantly contain chorus with rising tones and impulsive chorus. The corresponding parts of the Polar orbits are plotted in the solar magnetospheric (SM) coordinates in Figure 3 of *LeDocq et al.* [1998]. This carefully selected database of chorus events represents 20.2 hours of data with 7903 waveform snapshots that we use for further analysis.

[10] As the first step, we organize the data as a function of the $L*$ coordinate that is useful for a statistical description of chorus in relation to energetic electrons. $L*$ represents the radial distance in R_E to the intersection of the geomagnetic equatorial plane and the symmetric shell on which the electrons would occur, if we adiabatically removed non-dipolar components of the trapping magnetic field. It therefore takes into account all three adiabatic invariants. This "generalized L value" is defined by equation (4.24) of *Roederer* [1970, p. 107] as

$$L* = 2\pi B_D R_E^2 / \Phi, \tag{1}$$

where B_D is the dipole component of the surface magnetic field at the equator that we obtain from the International Geomagnetic Reference Field (IGRF) model, Φ is the magnetic flux encompassed by a guiding drift shell of trapped particles and depends also on the model of external contributions to the magnetic field, and R_E is the Earth radius.

[11] We calculate $L*$ for the spacecraft positions corresponding to all waveform snapshots during the chorus events. We use the ONERA-DESP library version 4.2 (D. Boscher et al., 2008) for the determination of Φ for locally mirrored electrons. When using the T89c model of the external component of the magnetic field [*Tsyganenko*,
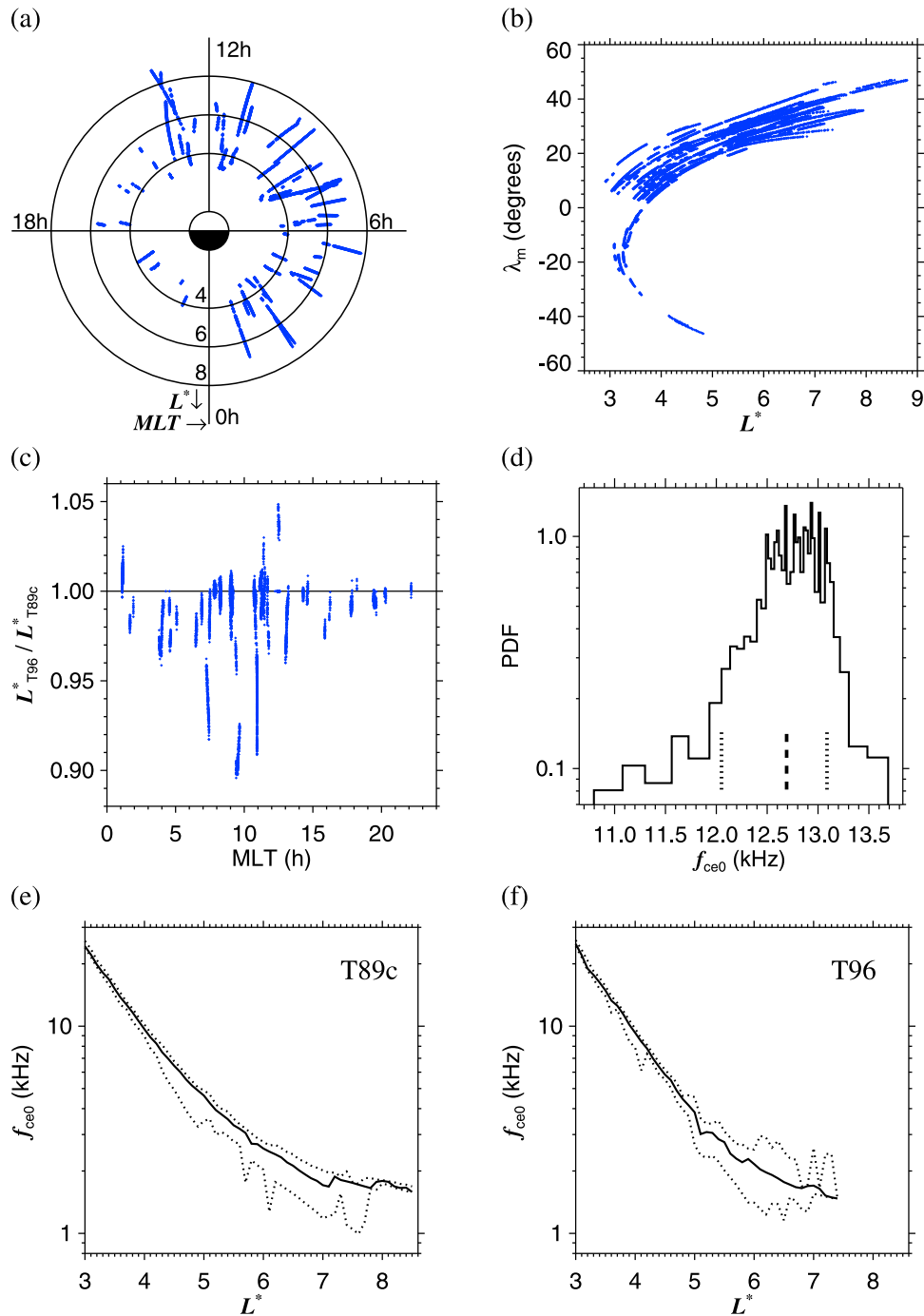
Figure 1. Positions of the spacecraft and minimum cyclotron frequencies for the chorus data set. (a) Polar plot of spacecraft positions in the L^* coordinate (see the text) and magnetic local time; (b) spacecraft positions in the plane defined by L^* and the magnetic latitude λ_m for all magnetic local times; (c) comparison of the L^* values obtained from the T96 and T89c magnetic field models as a function of magnetic local time; (d) probability density function of the minimum cyclotron frequency f_{ce0} along the field line passing through the spacecraft positions at $3.7 \leq L^* < 3.8$: the median value is marked by a thick dashed line, and the percentiles $Q_{-\sigma}$ and $Q_{+\sigma}$ are marked by thick dotted lines; (e) the minimum cyclotron frequency f_{ce0} as a function of L^* using the T89c model: the median value is shown by a solid line, and the percentiles $Q_{-\sigma}$ and $Q_{+\sigma}$ are plotted by dotted lines; and (f) similar to Figure 1e but using the T96 model.

1989], we have obtained results shown in Figures 1a and 1b. The data set has been slightly reduced to 7182 snapshots in 56 orbits for which closed drift shells have been found and $L*$ could be obtained. In Figure 1a spacecraft positions for these chorus snapshots are plotted onto the plane defined by the $L*$ coordinate and the magnetic local time (MLT). Our observations cover all MLT but there is only a small number of observations in the afternoon and evening sectors and they are confined to $L*$ lower than 6. In the MLT interval between 0100 and 1400 where chorus is usually observed we indeed find the absolute majority of measurements. They extend in $L*$ from 2.9 to 8.8. Note that there are only 2 chorus orbits for high values of $L* > 8$ but their number increases rapidly for lower $L*$: from 13 orbits for $7 < L* \leq 8$, to 32 orbits for $4 < L* \leq 5$.

[12] As a result of the highly inclined orbit of the spacecraft, the $L*$ values are linked to the magnetic latitude of observations (λ_m). This is documented in Figure 1b. A higher $L*$ generally corresponds to a higher λ_m. The spacecraft orbit also implies that chorus is seldom observed in the southern hemisphere (on negative λ_m). During the analyzed time interval, the perigee of the orbit was in the southern high-latitude region and the spacecraft moved down to and within the plasmasphere for most of the time spent at negative λ_m.

[13] Our calculations of the $L*$ parameter obviously depend on the particular model of the external magnetic field. The T89c model that we use in Figures 1a and 1b (and throughout the paper) is relatively simple and therefore computationally inexpensive, and its only input parameter is the Kp index that is always available. Newer models that are controlled by solar wind parameters, such as the T96 model [*Tsyganenko*, 1995] or by the solar wind parameters including their integrated history [e.g., *Tsyganenko and Sitnov*, 2005] are more accurate during magnetically disturbed conditions and in critical regions, such as in the vicinity of the dayside high-latitude magnetopause. Note, however, that our data set was recorded during predominantly quiet periods in the minimum of the solar cycle, with the maximum Kp index reaching only 5-, and with median values between 2- and 3- in the entire range of the obtained $L*$ values. To roughly estimate the precision of our $L*$ calculations, we compare the results from the T89c and T96 models in Figure 1c, as a function of magnetic local time. We can see that the results from the two models match within 5% accuracy most of the time (often with slightly lower values from the T96 model than from the T89c model), with the exception of a few orbits on the dawnside and dayside where the T89c model can give by up to approximately 10% larger values of $L*$ than the T96 model.

[14] Since whistler mode chorus is typically observed at frequencies that are a fraction of the electron cyclotron frequency in its source region, we need to estimate this frequency for every snapshot in our data set. As a reasonable approximation, we will use the minimum electron cyclotron frequency f_{ce0} along the magnetic field line passing through the point of observation. For each of the spacecraft positions corresponding to the chorus wave snapshots, we again use the T89c model and the ONERA-DESP library to determine the local electron cyclotron frequency f_{ce}^{M} and minimum electron cyclotron frequency f_{ce0}^{M} along a given model field

line. This model value is then recalibrated using the locally measured magnetic field strength and the corresponding local electron cyclotron frequency f_{ce},

$$f_{ce0} = f_{ce0}^{M} \frac{f_{ce}}{f_{ce}^{M}}. \tag{2}$$

The obtained values of f_{ce0} represent our estimates of the minimum electron cyclotron frequencies that are combined from experimental and model values.

[15] To obtain information on statistical properties of f_{ce0}, we use the same general procedure as for the wave parameters later in this paper. Here we describe this general procedure in detail using f_{ce0} as an example of input data. Every f_{ce0} value then has its corresponding $L*$, and we first bin the obtained f_{ce0} values in 56 equal $L*$ intervals between 3 and 8.6. In each of these bins we order the f_{ce0} values by their magnitude and rename this sequence to q_i, where i is an index from 1 to N, and N is the total number of values in a given $L*$ bin,

$$q_i \leq q_{i+1}, \quad i = 1 \ldots N - 1. \tag{3}$$

We then estimate a set of percentiles Q_p of the cumulative probability distribution using linear interpolation in this ordered sequence,

$$Q_p = q_{[\gamma]} + (q_{[\gamma]+1} - q_{[\gamma]})(\gamma - [\gamma]), \tag{4}$$

where $\gamma = pN + \frac{1}{2}$, and p is the probability that corresponds to a given percentile Q_p. The square brackets $[\gamma]$ denote the truncation operation to the nearest whole integer that is lower or equal to the argument γ. For every percentile Q_p we thus have $[pN]$ values in the sequence that are lower than Q_p. We define a set of 43 percentiles $Q_{j/K}$, where $j = 1 \ldots K - 1$, and $K = 44$. This number of percentiles is high enough to obtain a sufficient description of the probability distribution. For example, we have

$$Q_m = Q_{0.5} \qquad (\text{for } j = 22),$$

$$Q_{-\sigma} = Q_{0.159} \qquad (\text{for } j = 7), \tag{5}$$

$$Q_{+\sigma} = Q_{0.841} \qquad (\text{for } j = 37),$$

where Q_m corresponds to an estimate of the median value, and $Q_{-\sigma}$ and $Q_{+\sigma}$ correspond to the mean value minus or plus one standard deviation, respectively, if the underlying probability distribution is normal. From $Q_{-\sigma}$ and $Q_{+\sigma}$ we have

$$\sigma = \frac{1}{2}(Q_{+\sigma} - Q_{-\sigma}), \tag{6}$$

where σ is equal to the standard deviation if the underlying probability distribution is normal, but it can always serve as a measure of variability for an arbitrary probability distribution.

[16] Figure 1d shows an example of results of this procedure for the values of the minimum cyclotron frequency f_{ce0} (equation (2)) in the $L*$ bin between 3.7 and 3.8 where we obtain a total number of 808 data points corresponding to waveform snapshots in 15 orbits when chorus was

observed. The probability density function (PDF) is estimated from the 43 percentiles $Q_{j/K}$ values using

$$\mathrm{PDF}(x) = \frac{1}{K}\left(Q_{(j+1)/K} - Q_{j/K}\right)^{-1}$$
$$\text{for} \quad Q_{j/K} \le x < Q_{(j+1)/K}, \quad j = 1 \ldots K-1$$

$$\mathrm{PDF}(x) = 0$$
$$\text{for} \quad x < Q_{1/K} \ \text{and} \ x \ge Q_{(K-1)/K}, \tag{7}$$

where we have $x = f_{ce0}$ in this case. The median value Q_m and the percentiles $Q_{-\sigma}$ and $Q_{+\sigma}$ (equation (5)) are also shown in Figure 1d. The probability density function is slightly skewed, with more variability for lower f_{ce0}, but still it is well concentrated around the median value. The mean value of 12.6 kHz estimated from

$$\mu = \int_{-\infty}^{\infty} x\,\mathrm{PDF}(x)\,dx \approx \frac{1}{K-1}\sum_{j=1}^{K-1} Q_{j/K} \tag{8}$$

is thus close to the median value of 12.7 KHz.

[17] The median value Q_m and the percentiles $Q_{-\sigma}$ and $Q_{+\sigma}$ of the minimum cyclotron frequency f_{ce0} are shown in Figure 1e in the L^* bins between 3 and 8.6 for all the intervals when chorus was observed. At higher L^* we also observe a larger variability expressed by the difference between $Q_{-\sigma}$ and $Q_{+\sigma}$. Comparing these results of the f_{ce0} calculation with the T96 model (shown in Figure 1f), we can note a similar scaling of the median value but with a lower number of data points spanning only up to $L^* = 7.4$. Note that individual values of f_{ce0} from the T96 model are usually within 10%–20% from those obtained using the T89c model, but in a few orbits they can be different by a larger factor of 0.6–1.7. These differences are not critical for our analysis since we only use median values for comparison with the wave frequencies.

[18] After this initial analysis, the chorus waveform snapshots are organized as a function of the L^* coordinate and a statistical description of the corresponding f_{ce0} values is obtained. Next, we analyze the six-component waveform snapshots as a function of frequency. We use the fast Fourier transform on three windowed segments per snapshot with 50% overlapping. This leads to averaged Hermitian spectral matrices 6×6 obtained with a frequency resolution of 4.5 Hz. These spectral matrices are further averaged and attributed to 32 logarithmic frequency bins between 100 Hz and 25 kHz with 19% ($\Delta f/f$) steps.

[19] Combining these frequency bins with the above described 56 equal intervals of L^* between 3 and 8.6, we obtain a 2-D grid in the L^*-frequency plane. In each 2-D bin in this grid, we have a large number of spectral matrices (typically several hundreds) containing information on the power, mutual phases and coherency of the electric and magnetic field components.

3. Probability Density Functions of Chorus Power Spectral Densities

[20] Figure 2 shows results of analysis of power spectral densities of the magnetic field and electric field in the L^*-frequency plane. We have used the same definition of

bins and the same analysis method of the multicomponent waveform snapshots as we have described in section 2. From each resulting spectral matrix we have first calculated the sum of the power spectral densities from three orthogonal magnetic antennas S_B and a similar sum from three orthogonal electric components S_E. These values have been analyzed to obtain the set of percentiles Q_p according to equation (4). Figures 2a and 2b show the median values Q_m (equation (5)) for S_B and S_E, respectively.

[21] In Figures 2a and 2b we can see a band of more intense median power spectral densities around the overplotted black line that shows one half of the median f_{ce0} from Figure 1e. This band corresponds to chorus emissions that mainly occur below $\frac{1}{2} f_{ce0}$. Note that the median S_B increases with L^* in the chorus band in Figure 2a. This effect is observed for the dayside orbits with MLT between 0800 and 1600 (not shown) while its existence is unclear on the nightside and dawnside. The very high median values at $L^* > 7.5$ are however less reliable than results at $L^* \le 7.5$ since the orbital coverage is low in this region and we obtain only $\approx$50–200 spectral matrices per bin compared to 300–1000 spectral matrices per bin at $L^* \le 7.5$.

[22] The chorus band is also clearly seen in Figures 2c and 2d which show the results for σ from equation (6). Even if the underlying distribution is far from being normal (as we will show), this values provide us with a measure of variability of S_B and S_E. The chorus band is more pronounced in Figures 2c and 2d than when we look at the median values in Figures 2a and 2b. This means that the chorus intensity is highly variable from case to case. Note again that σS_B gradually increases with L^* in the chorus band in Figure 2c.

[23] To investigate the nature of the variability of chorus power spectral densities we analyze their probability distributions. Figures 2e and 2f show examples of estimates of the probability density functions of S_B and S_E for an L^*-frequency bin in the chorus band at $6.9 \le L^* < 7.0$, and at frequencies between 340 and 400 Hz. We use the procedure described by equation (7) for 454 spectral matrices collected during 13 orbits. The results are very different from the approximately normal distribution of f_{ce0} in Figure 1d. The consequence is that the mean values from equation (8) are approximately 1 order of magnitude higher than the median values (equation (5)) shown on the bottom of Figures 2e and 2f. The PDFs of S_B and S_E approximately follow a power law

$$\mathrm{PDF}_p(x) = C x^{-\alpha}, \quad x > x_0, \tag{9}$$

where we use S_B and S_E in place of x and we obtain α close to or slightly above 1 in Figures 2e and 2f. This shape of the PDF is typical for the entire chorus band although the details and the values of the exponent α may vary.

[24] Note that equation (9) fits the PDF of S_B over the range $S_B > 9 \times 10^{-9}$ nT^2 Hz^{-1} while the same fit for S_E is valid when $S_E > 3 \times 10^{-5}$ mV^2 m^{-2} Hz^{-1}. This a general property of the power law distributions that can only describe the tail of the PDF above a threshold x_0 [Newman, 2005; Clauset et al., 2009]. An alternative model of the observed "heavy tail" distributions can be the lognormal distribution,

$$\mathrm{PDF}_l(x) = \frac{1}{x\sigma_L\sqrt{2\pi}}\exp\left[-\frac{(\ln x - \mu_L)^2}{2\sigma_L^2}\right], \quad x > 0, \tag{10}$$
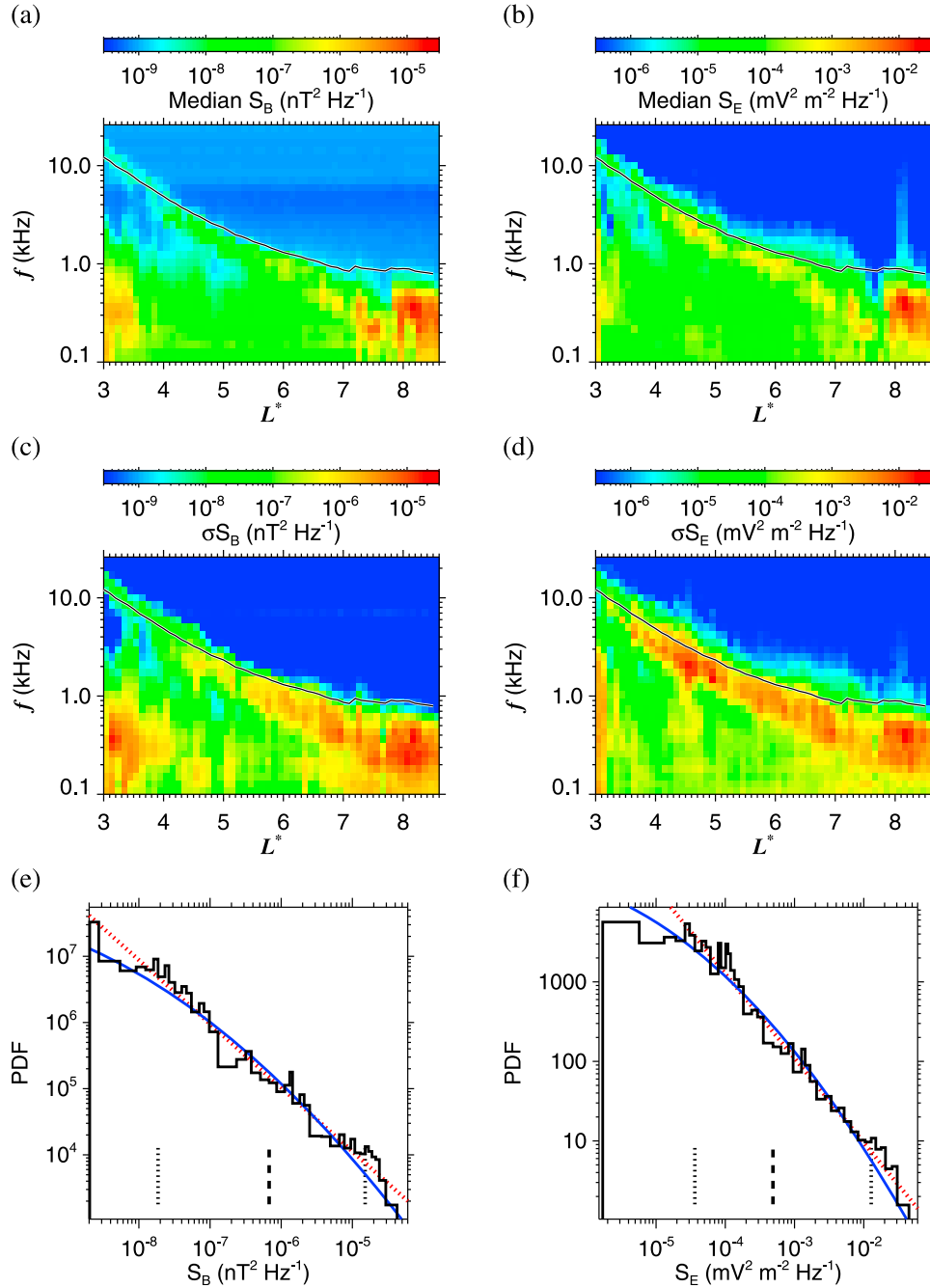
Figure 2. Power spectral densities of the magnetic field and electric field. (a) Median value of the sum of the power spectral densities from three orthogonal magnetic antennas; the overplotted black line shows one half of the median f_{ce0} from Figure 1e. (b) The same as Figure 2a but for three orthogonal electric components. (c) One half of the difference between the percentiles $Q_{+\sigma}$ and $Q_{-\sigma}$ (σ from equation (6)) as a measure of variations of the sum of power spectral densities from the magnetic antennas. (d) The same as Figure 2c but for the electric components. (e) Example of the probability density function (PDF) of the sum of the power spectral densities from the three magnetic antennas (solid black line), analyzed for $6.9 \leq L^* < 7.0$, and at frequencies between 340 and 400 Hz; the median value is marked by a thick dashed vertical line, and the percentiles $Q_{-\sigma}$ and $Q_{+\sigma}$ are marked by thick dotted vertical lines on the bottom. Fits of the power law and lognormal models are shown by the red dotted and blue solid lines, respectively. (f) The same as Figure 2e but for the three electric components.

where we use parameters

$$\mu_L = \ln Q_m$$

$$\sigma_L = \frac{1}{2}(\ln Q_{+\sigma} - \ln Q_{-\sigma}) \tag{11}$$

from equation (5). Figures 2e and 2f show that the lognormal and power law models give similar answers above x_0 and that the tail of the distribution seems to be modeled equally well by both models.

[25] Measurements of full vectors of fluctuating electric and magnetic fields allow us to calculate the spectral density of the modulus of the Poynting vector S_S using the spectral matrices 6×6,

$$S_{S1} = \frac{1}{\mu_0}(\Re S_{E2B3} - \Re S_{E3B2})$$

$$S_{S2} = \frac{1}{\mu_0}(\Re S_{E3B1} - \Re S_{E1B3})$$

$$S_{S3} = \frac{1}{\mu_0}(\Re S_{E1B2} - \Re S_{E2B1}) \tag{12}$$

$$S_S = \sqrt{S_{S1}^2 + S_{S2}^2 + S_{S3}^2},$$

where $\Re S_{EiBj}$ are real parts of the cross-power spectra between components of the electric and magnetic fields, S_{Sk} are spectral densities of the effective values of components of the Poynting vector (i, j, $k = 1\ldots3$), and μ_0 is the permeability of free space.

[26] The obtained values of S_S have been subjected to the same analysis as the power spectral densities of the electric and magnetic fields shown in Figure 2. Median values of S_S in the L^*-frequency plane are plotted in Figure 3a and, as a measure of variability of S_S we show the corresponding σ obtained from equation (6) in Figure 3c. Chorus band is again clearly apparent in both Figures 3a and 3c. We can also note that both the median and σ of S_S gradually increase with L^* in the chorus band. This effect is again clearly observed for the dayside orbits (not shown).

[27] Figure 3e shows an example of the PDF calculated using equation (7) from the same L^*-frequency bin as in Figures 2e and 2f. This PDF gives an estimate of the mean value of 0.1 nW m^{-2} Hz^{-1} (equation (8)), approximately 1 order of magnitude higher than the median value shown on the bottom of Figure 3e. The lognormal distribution fits well the PDF of the Poynting flux in the entire range of obtained values, but a similarly good fit is also obtained above a threshold of 2×10^{-4} nW m^{-2} Hz^{-1} using the power law model with α close to 1.

[28] In the subsequent analysis we will use two threshold values for S_S. The first threshold is used to filter out only the weakest waves outside the chorus band. It is therefore selected 1 order of magnitude below the range of the obtained chorus values, at $S_S > 10^{-6}$ nW m^{-2} Hz^{-1}. The second threshold will be used to analyze only the strongest waves, with $S_S > 10^{-3}$ nW m^{-2} Hz^{-1}.

[29] To ensure the presence of right-hand polarized whistler mode waves we also use a threshold for ellipticity of polarization of the magnetic field fluctuations. We calculate it using the singular value decomposition (SVD) of the magnetic part of the spectral matrix [*Santolík et al.*, 2003b, equation (13)]. We additionally define the sign of

the ellipticity by the sense of polarization [see *Santolík et al.*, 2002, appendix]; positive values mean the right-hand polarization and negative values are used for the left-hand polarization. A negligible absolute value of the ellipticity means that the polarization is linear, while an absolute value close to one means circular polarization.

[30] Results of this calculation are shown in Figures 3b and 3d in a similar format as we have used in Figures 3a and 3c. In the chorus band we obtain the right-hand, nearly circular magnetic field polarization with very low level of fluctuations. At higher frequencies where only a low-intensity noise is observed the ellipticity is random and the empty regions indicate bins where we obtain less than 12 spectral matrices with $S_S > 10^{-6}$ nW m^{-2} Hz^{-1}. Figure 3f shows the PDF of the ellipticity values in the same L^*-frequency bin as we have used for Figure 3e. Since this bin is contained in the chorus band, the major peak of the PDF is concentrated at high positive values close to 1. In our analysis all spectral matrices with ellipticities lower than a threshold of $+0.2$ are excluded and only the right-hand polarized waves are thus taken into account. This threshold is used for Figures 1, 2, 3a, 3c, 3e, and 4 but not those that show the ellipticity itself (Figures 3b, 3d, and 3f).

4. Propagation of Chorus in the Outer Zone

[31] From the spectral densities of components of the Poynting vector (equation (12)) we can also estimate the angle θ_S' of the Poynting vector with respect to the direction of the static magnetic field $\mathbf{B}_0$. If we define the $S3$ axis along $\mathbf{B}_0$ we obtain

$$\theta_S' = \arctan\left(\frac{\sqrt{S_{S1}^2 + S_{S2}^2}}{S_{S3}}\right), \tag{13}$$

where θ_S' ranges between 0 (when the Poynting vector is parallel to $\mathbf{B}_0$) and π (when the Poynting vector is antiparallel to $\mathbf{B}_0$). To determine if the waves propagate away from the magnetic equator or toward the equator we need to take into account information on the magnetic hemisphere of the point of observation. We obtain it from the ONERA-DESP library using the IGRF and T89c models of the magnetic field. We then define angle θ_S

$$\theta_S = \theta_S' \quad \text{in the northern hemisphere}$$

$$\theta_S = \pi - \theta_S' \quad \text{in the southern hemisphere,} \tag{14}$$

where $\theta_S = 0$ if the waves propagate with the Poynting vector parallel to the magnetic field line away from the magnetic equator toward the Earth. $\theta_S = \pi$ when the Poynting vector is parallel to the magnetic field line and toward the magnetic equator, away from the Earth.

[32] Figure 4 shows the analysis of the obtained θ_S values (converted to degrees) in the same format as we have used in Figures 2 and 3. Figures 4a, 4c, and 4e use the threshold for the absolute value of the Poynting flux $S_S > 10^{-6}$ nW m^{-2} Hz^{-1} while Figures 4b, 4d, and 4f are plotted for intense waves with $S_S > 10^{-3}$ nW m^{-2} Hz^{-1}. Empty regions again indicate bins where we obtain less than 12 spectral matrices after using one of these two thresholds for S_S and the ellipticity threshold described in section 3. In Figures 4a and 4b we
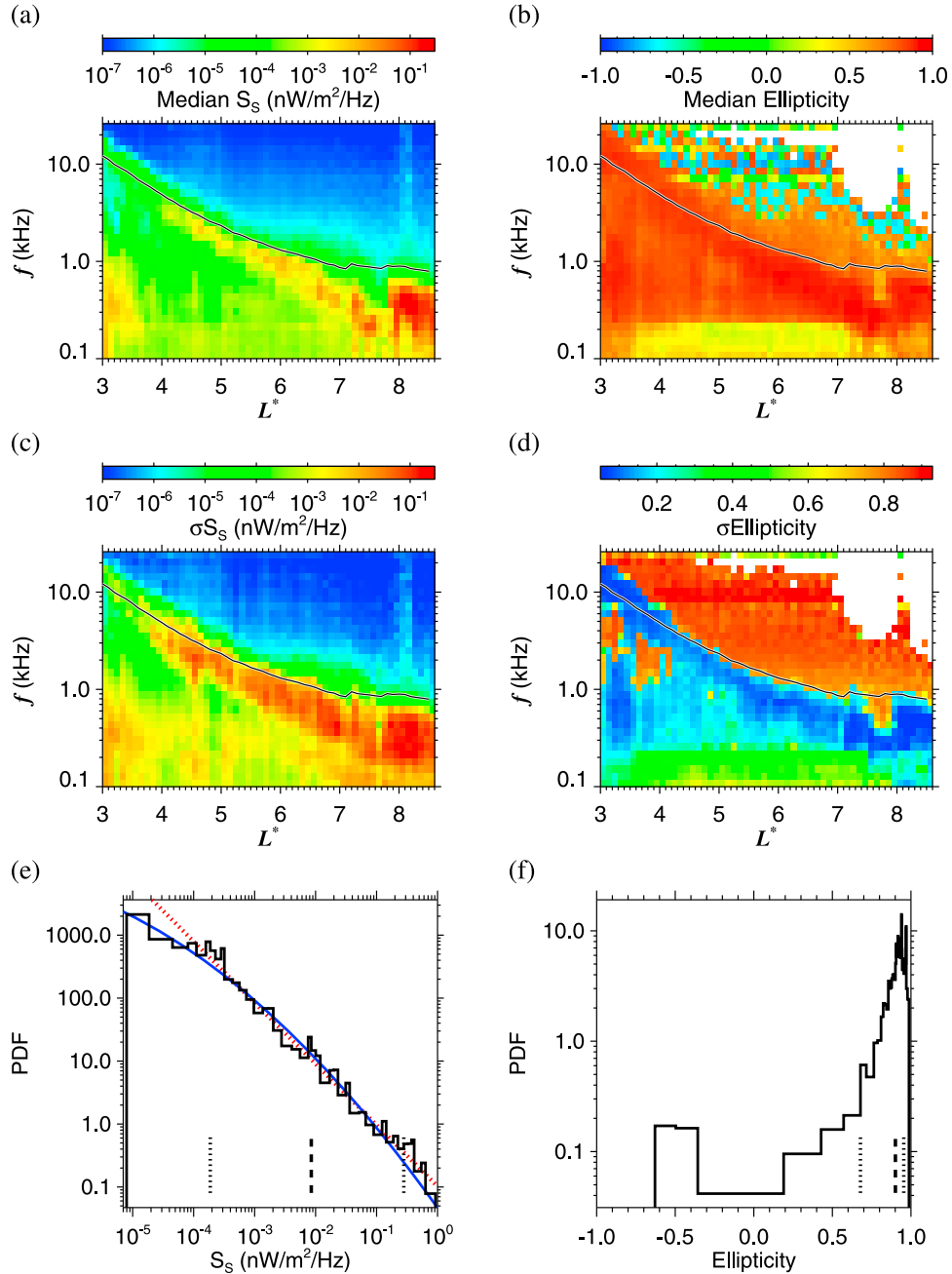
Figure 3. Spectral density of the Poynting flux and the ellipticity of magnetic field fluctuations in the same format as in Figure 2. (a) Median value of the spectral density of the Poynting flux; (b) median value of the ellipticity of magnetic field fluctuations; (c) one half of the difference between the percentiles $Q_{+\sigma}$ and $Q_{-\sigma}$ as a measure of variations of the spectral density of the Poynting flux; (d) the same as Figure 3c but for the ellipticity of magnetic field fluctuations; (e) example of the probability density function (PDF) of the spectral density of the Poynting flux of chorus, analyzed for $6.9 \leq L* < 7.0$ and at frequencies between 340 and 400 Hz; and (f) the same as Figure 3e but for the ellipticity of magnetic field fluctuations.

can clearly recognize the main chorus band, propagating away from the equator with median values of $\theta_S < 20°$–30°. The chorus band also shows low fluctuations, $\sigma\theta_S < 10°$–20°, in Figures 4c and 4d.

[33] Our analysis allows us to investigate also other types of waves that are colocalized with chorus and/or propagate at similar frequencies. At lower frequencies and lower $L*$

than the main chorus band, we obtain waves whose median $\theta_S > 120°$–150° (Figure 4a), indicating propagation toward the equator. The variability of obtained θ_S values is however large (Figure 4c), especially close to the lower boundary on the main chorus band where waves propagating from the equator are also often observed but, as the median value in Figure 4a indicates, waves with equatorward propagation
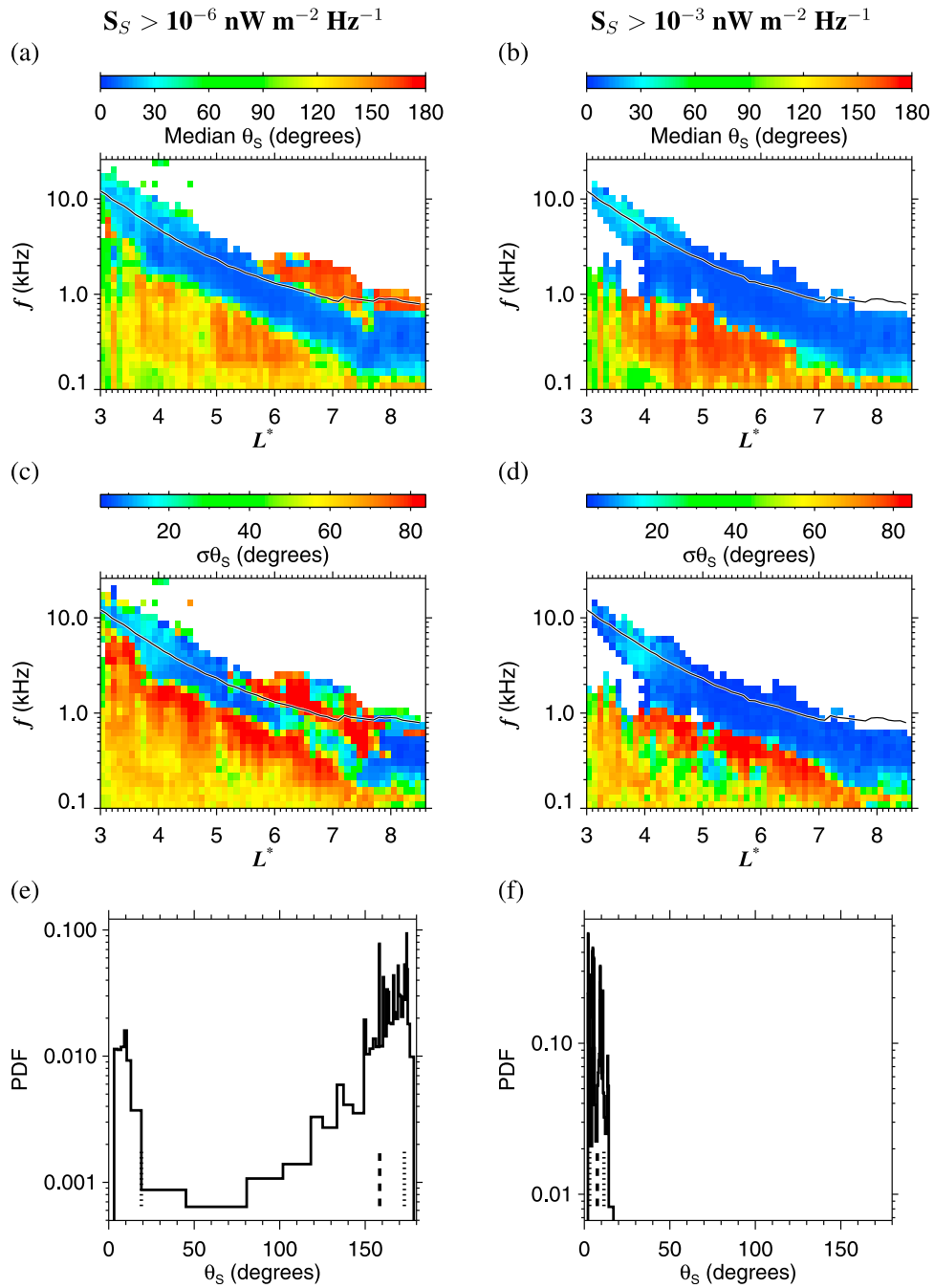
Figure 4. Angle θ_S between the Poynting vector and the static magnetic field $\mathbf{B}_0$ analyzed using the same methods and plotted in the same format as in Figures 2 and 3. (a) Median value of θ_S for cases when the spectral density of the Poynting flux S_S is larger than the noise level of 10^{-6} nW m^{-2} Hz^{-1}; (b) the same as Figure 4a but for $S_S > 10^{-3}$ nW m^{-2} Hz^{-1}; (c) one half of the difference between the percentiles $Q_{+\sigma}$ and $Q_{-\sigma}$ as a measure of variations of θ_S for $S_S > 10^{-6}$ nW m^{-2} Hz^{-1}; (d) the same as Figure 4c but for $S_S > 10^{-3}$ nW m^{-2} Hz^{-1}; (e) the probability density function (PDF) of θ_S, analyzed for $6.9 \leq L^* < 7.0$ and for frequencies between 960 and 1140 Hz, when $S_S > 10^{-6}$ nW m^{-2} Hz^{-1}; and (f) the same as Figure 4e but when $S_S > 10^{-3}$ nW m^{-2} Hz^{-1}.

prevail. This picture becomes clearer when we analyze selected intense waves with $S_S > 10^{-3}$ nW m^{-2} Hz^{-1}. The median value of θ_S is above 150° in the region of the L^*-frequency plane below the main chorus band (Figure 4b) and the large variability is only observed at the contact of this region with the main chorus band (Figure 4d).

[34] In the outer zone for $L^* > 6$ we observe another wave class propagating away from the Earth and toward the equator at frequencies above the main chorus band. Figure 4a shows that median values of θ_S for these waves are above 150°, with a pronounced variability at the contact with the main chorus band. A region of lower variability (Figure 4b)

can be found at slightly higher frequencies above 1 kHz and at L^* close to 7. In the vicinity of $\frac{1}{2}f_{ce0}$ the prevailing direction of the Poynting vector is still equatorward as it is also documented by the PDF of θ_S calculated according to equation (7) and shown in Figure 4e. The observed high variability of θ_S is explained by the presence of two peaks in the PDF. One belongs to the waves from the main chorus band propagating at $\theta_S < 20°$. The other, more pronounced one, is found at $\theta_S > 150°$. Their simultaneous presence causes a large difference of the percentiles $Q_{+\sigma}$ and $Q_{-\sigma}$ shown on the bottom of Figure 4e, and hence large values of σ according to equation (6). The waves propagating toward the equator occur more often, as is reflected by the high median value of θ_S in this L^*-frequency bin (also shown on the bottom of Figure 4e).

[35] These waves are however much weaker than the main chorus band propagating away from the equator. This is documented by the total absence of the outer zone equatorward propagating emissions in Figures 4b, 4d, and 4f. Analysis using different S_S thresholds (not shown) indicates that some residual signs of these waves can still be seen up to a threshold of $S_S > 10^{-4}$ nW m^{-2} Hz^{-1} but that they mostly disappear at a level of $S_S \approx 10^{-5}$ nW m^{-2} Hz^{-1}.

5. Discussion and Conclusions

[36] Several aspects of our procedure need to be discussed before we can draw conclusions from this study. Together with the study of *Sigsbee et al.* [2010] in the same special issue on chorus emissions, this is, to our knowledge, the first analysis of wave emissions in the inner magnetosphere that is parameterized by the L^* coordinate according to equation (1).

[37] We have shown (Figure 1c) that the differences of L^* that we obtain using different models of the external magnetic field are typically a few percent. This difference is small enough that it does not affect our results, being comparable to the bin size used in the statistical analysis. We have therefore chosen to use the older T89 model because it is computationally inexpensive, and, more importantly, because it uses the easily accessible Kp index as its input. The newer models need solar wind measurements that are not always available and therefore these models considerably reduce our data set. For example, the T96 model reduces the data set from 7182 spectral matrices down to only 4380 spectral matrices that were measured when the solar wind data were available. The modern models that use the integrated history of the solar wind parameters [e.g., *Tsyganenko and Sitnov*, 2005] would reduce our data set even more.

[38] Note that another parameter, the dipole L, has been used in many previous studies of whistler mode chorus based on the measurements of the CRRES spacecraft [*Meredith et al.*, 2001, 2002, 2003a, 2003b, 2009], or the Double Star and CLUSTER spacecraft [*Santolík et al.*, 2005; *Pokhotelov et al.*, 2008]. It is defined as

$$L = R/\cos^2(\lambda_m), \tag{15}$$

where R is the radial distance and λ_m is the magnetic latitude. This definition is clearly different from equation (1) and leads to a very simple and straightforward calculation

that, however, gives remarkably different results in the outer zone: the relative difference of L and L^* can typically reach several tens percent in the outer radiation belt at $L^* > 5$ (it means, mainly outside of the range of the CRRES data). For example, in our data set the dipole L values span from 3.0 to 11.8, with 10 orbits extending to $L > 8$, while L^* values only range from 2.9 to 8.8, with 2 chorus orbits at $L^* > 8$.

[39] Yet another method has been used by *Li et al.* [2009] to characterize the occurrence rates of chorus observed by the THEMIS spacecraft; they mapped data measured at different magnetic latitudes to the magnetic equator using the T96 magnetic field model and their L value was obtained as the radial distance from the center of the Earth to the equatorial crossing point. On the dayside this method gives slightly lower values than the dipole model (equation (1)) but compared to L^* values calculated from equation (1), the method of *Li et al.* [2009] always gives higher values in our data set. A typical relative difference at $L^* > 5$ reaches 20%–50%. For example, at $6.9 < L^* < 7.1$ we obtain, using the method of *Li et al.* [2009], L between 7.3 and 9.6, with the median value of 8.6.

[40] Looking at these nonnegligible differences, it appears recommendable to use L^* in future statistical studies of waves that can affect the trapped energetic particles in the inner magnetosphere because L^* is better suited for the parameterization of the trapped radiation [*Roederer*, 1970].

[41] It is also clear that only a rough comparison of our results with previous studies can be done. Our results show both increasing median value and variability of S_B as a function of L^* in Figures 2a and 2b. For the observed nonnormal distributions the mean value increases with both the corresponding median and σ values. Hence, we also obtain increasing mean values as a function of L^* (not shown). This result confirms the first observations of a similar phenomenon by the Double Star TC-1 spacecraft [*Santolík et al.*, 2005], and results of *Li et al.* [2009], who found a similar effect in the data of the THEMIS spacecraft.

[42] *Li et al.* [2009] and many previous studies investigate the MLT and latitudinal dependence of chorus intensities and occurrence rates. We neither attempt to systematically analyze the MLT nor latitudinal dependence of chorus intensities since our data set is limited and the statistics would be poor. Instead, we concentrate on two important aspects of the analysis of spatial distribution of chorus: we investigate the statistical properties (probability distributions) of chorus power spectral densities and we use the combined measurements of the wave magnetic and electric field to estimate the Poynting vector of chorus.

[43] Our initial results concerning the probability distributions of power spectral densities of chorus show that it might be misleading to use the average values to fully characterize chorus intensities, as it is done in all previous studies. We find lognormal probability distributions with large variances and hence with the heavy tail features or, alternatively, power law probability distributions with low exponents. *Newman* [2005] has shown that the two types of distributions can be very similar over a large range of values and that it may be difficult to distinguish between these two models. We do not attempt to do it rigorously, for example using the Kolmogorov-Smirnov statistics, since simulation studies show that the limited size of our data set is probably insufficient for this task [*Clauset et al.*, 2009]. Future studies

will certainly be needed to resolve this problem which is far from being trivial. Its consequences are clearly related to the model of chorus generation. If the hypothesis of the log-normal probability distribution is proven, a model similar to the stochastic growth theory of Langmuir waves in the solar wind [*Cairns and Robinson*, 1999] would possibly provide us with a plausible physical interpretation. On the other hand, only more complex nonlinear models of chorus gen-eration can explain the power law distributions. In this case, the obtained low exponents ($\alpha < 2$) also imply that the widely used average values have a questionable physical interpretation and depend on the size of the underlying data set.

[44] Our analysis of the directions of the Poynting vector of chorus (Figure 4) confirms the original result of *LeDocq et al.* [1998] that the main chorus band in this Polar data set systematically propagates away from the equatorial surface, where the magnetic field strength in minimum along a given field line. We succeed to add two significant components to this result: the waves below the main chorus band in the $L*$-frequency plane, and the outer zone emissions above the main chorus band in the $L*$-frequency plane, both propagate toward this surface. These wave emissions were not subject of analysis of *LeDocq et al.* [1998].

[45] Properties of the waves that we observe below the main chorus band are very similar to events of reflected chorus (with only residual structure of discrete wave pack-ets) described in the case studies based on the measurements of the Cluster spacecraft by *Parrot et al.* [2003b, 2004]. Here we show, using the Polar data set, that this phenom-enon occurs systematically. Ray tracing analysis of cases reported by *Parrot et al.* [2003b, 2004] has shown that reflected chorus can occur closer to the Earth than the original chorus emission and our statistical results agree with this conclusion.

[46] On the other hand, the outer zone waves above the main chorus band are observed further from the Earth than waves at the same frequencies in the main chorus band. This interesting class of emissions therefore cannot be related to the inward reflected chorus according to the ray tracing studies by *Parrot et al.* [2003b, 2004]. We can then explain their propagation by a poleward reflection of equatorial chorus described by a theoretical ray-tracing study of *Chum and Santolík* [2005] and experimental observations of *Santolík and Parrot* [2000] and *Santolík et al.* [2006]. Chorus would, in these cases, propagate to higher $L*$.

[47] On the dayside, this outer zone chorus can be attributed to pockets of low magnetic field strength (mini-mum-B pockets) as it was first proposed by *Tsurutani and Smith* [1977]. This would correspond well to the predomi-nant occurrence of outer zone chorus during geomagneti-cally quiet periods reported by *Tsurutani and Smith* [1977]: our data set was recorded during the minimum of the solar cycle with a predominant occurrence of quiet periods. In this case its wave frequency should not be compared with $\frac{1}{2}f_{ce0}$ since the proper value of the electron cyclotron frequency in source region may be different. A preliminary analysis of high-resolution spectrograms based on the Polar waveform measurements (not shown) indicates the presence of chorus-like structures resembling a sequence of discrete wave packets in these outer zone emissions.

[48] There are two potential problems with this explana-tion: First, the observed outer zone waves propagating from the Earth are much weaker than the main chorus band propagating toward the Earth. This is indeed the case in the OGO 5 data set [*Tsurutani and Smith*, 1977, Figure 10] who report that the high-latitude chorus is generally weaker but it disagrees with the case study of a Geotail high-latitude chorus event which had high-intensity subelements/wave packets [*Verkhoglyadova et al.*, 2009; *Tsurutani et al.*, 2009] and with the study of *Horne et al.* [2005], who found increasing wave amplitudes as a function of the magnetic latitude. Second, we observe the outer zone waves on the dayside as well as on the morning side at MLT < 8 hours (not shown), while chorus of *Tsurutani and Smith* [1977] is localized on the dayside. Both problems can be speculatively explained by possible propagation of chorus from its source region during which the waves are Landau damped or, alternatively, only a small fraction of their Poynting flux is reflected and allowed to reach the space-craft. This could still be consistent with the results for events of *Parrot et al.* [2003b, 2004] which depend on the partic-ular magnetic field configuration and on the set of initial wave vector directions in the chorus source region. More work is needed to reliably identify the origin of the equa-torward propagating outer zone waves.

[49] Our analysis of the total Poynting flux in the main chorus band (propagating away from the equator) provides us with another significant new result: We find that not only the previously reported magnetic field amplitudes but also the Poynting flux of chorus increases with $L*$ toward the outer zone at $L* > 6$.

[50] Using the measured Poynting flux we can further-more roughly estimate if chorus in the outer zone carries enough power to accelerate electrons in the outer Van Allen radiation belt to relativistic energies. The result, however, needs to be taken with caution as a very crude calculation of the energetic balance of chorus. Assumptions of this esti-mate may not correspond to the actual acceleration mechanism that is still not fully known and that may significantly depend on probability distributions of chorus amplitudes. At $L* \approx 6$–7 we have estimated the mean value of the spectral density of the Poynting flux of chorus to be 0.1 nW m^{-2} Hz^{-1} (see the text related to Figures 3a and 3e). The chorus band at this $L*$ is approximately 500 Hz wide (Figure 3a) which means that the total Poynting flux is $\approx 5 \times 10^{-8}$ W m^{-2}.

[51] The typical flux of electrons at energies ≥ 1 MeV in the outer radiation belt is assumed on the order of 10^6 cm^{-2} s^{-1}. This very roughly gives a number density of ≈ 30 m^{-3}. If we want to accelerate these particles from the plasma sheet energies up to 1 MeV we need to deposit an energy density of $\approx 5 \times 10^{-12}$ J m^{-3}. Now, assuming a field-aligned column of particles with a length of 3 Earth radii, we need a column-integrated energy density of $\approx 10^{-4}$ J m^{-2}. This value would be similar within a small factor of 2–3 if we consider a different column length comparable with a reasonable fraction of the total length of the magnetic field line. Therefore, we would need a time interval of ≈ 30 min to accumulate this column-integrated energy density from all the available average Poynting flux of chorus. If only a small part (approximately 1%) of the available Poynting flux is used to accelerate relativistic particles, we obtain the usual

timescale of days for changes of relativistic electron fluxes in the outer radiation belt.

[52] Finally, the conclusions of this work are as follows.

[53] 1. Our analysis of whistler mode chorus using the Polar measurements selected by *LeDocq et al.* [1998] shows that the $L*$ coordinates for this data set are different by tens of percent from the results obtained using different definitions of the L parameter that occur in the literature. Since the $L*$ coordinate is better suited for a description of trapped electrons, this result can have an impact on the way that the wave components of future models of the Van Allen radiation belts will be analyzed.

[54] 2. The power spectral density of the electric and magnetic field fluctuations carried by chorus has a probability distribution that is very far from being normal. The same holds true for the spectral density of the Poynting flux. The probability distribution has a heavy tail that can be described either by the lognormal distribution or by the power law distribution with a low exponent α that is close to (but larger than) 1. Our data set is insufficient to distinguish between these two possibilities. This can represent a significant input for the theories of chorus generation by an analogy of the stochastic growth theory [*Cairns and Robinson*, 1999] or by a nonlinear model. Another consequence of the heavy tail distributions is that the usual statistical characterization of chorus using arithmetic averages may have a questionable physical interpretation.

[55] 3. We find that the Poynting flux in the main chorus band on the dayside increases with $L*$ toward the outer zone at $L* > 6$. A rough estimate shows that outer zone chorus carries enough power to accelerate electrons in the outer Van Allen radiation belt to relativistic energies on a timescale of days: only a fraction on the order of 1% of the average Poynting flux needs to be deposited into the radiation belts to account for typical fluxes of relativistic electrons.

[56] 4. Statistical analysis of probability density functions of the angle θ_S describing the direction of the Poynting vector allows us to confirm that the main chorus band propagates away from the equator, as it was originally found by *LeDocq et al.* [1998]. We are also able to show the systematic occurrence of the magnetospherically reflected component of chorus found by case studies of *Parrot et al.* [2003b, 2004].

[57] 5. We observe outer zone waves that propagate toward the equator at larger frequencies than waves in the main chorus band. We propose a possible explanation by poleward reflection of equatorial chorus or dayside chorus of *Tsurutani and Smith* [1977].

References

Albert, J. M. (2008), Efficient approximations of quasi-linear diffusion coefficients in the radiation belts, *J. Geophys. Res.*, *113*, A06208, doi:10.1029/2007JA012936.

Bortnik, J., R. M. Thorne, and N. P. Meredith (2008), The unexpected origin of plasmaspheric hiss from discrete chorus emissions, *Nature*, *452*, 62–66, doi:10.1038/nature06741.

Bortnik, J., W. Li, R. M. Thorne, V. Angelopoulos, C. Cully, J. Bonnell, O. Le Contel, and A. Roux (2009), An observation linking the origin of plasmaspheric hiss to discrete chorus emissions, *Science*, *324*, 775–778, doi:10.1126/science.1171273.

Burtis, W. J., and R. A. Helliwell (1969), Banded chorus: A new type of VLF radiation observed in the magnetosphere by OGO 1 and OGO 3, *J. Geophys. Res.*, *74*, 3002–3010, doi:10.1029/JA074i011p03002.

Cairns, I. H., and P. A. Robinson (1999), Strong evidence for stochastic growth of Langmuir-like waves in Earth's foreshock, *Phys. Rev. Lett.*, *82*(15), 3066–3069, doi:10.1103/PhysRevLett.82.3066.

Chum, J., and O. Santolík (2005), Propagation of whistler-mode chorus to low altitudes: Divergent ray trajectories and ground accessibility, *Ann. Geophys.*, *23*, 3727–3738.

Clauset, A., C. Rohilla Shalizi, and M. E. J. Newman (2009), Power-law distributions in empirical data, *SIAM Rev.*, *51*, 661–703.

Gurnett, D. A., et al. (1995), The Polar Plasma Wave Instrument, *Space Sci. Rev.*, *71*, 597–622.

Hikishima, M., S. Yagitani, Y. Omura, and I. Nagano (2009), Full particle simulation of whistler-mode rising chorus emissions in the magnetosphere, *J. Geophys. Res.*, *114*, A01203, doi:10.1029/2008JA013625.

Horne, R. B. (2007), Acceleration of killer electrons, *Nat. Phys.*, *3*, 590–591.

Horne, R. B., R. M. Thorne, S. A. Glauert, J. M. Albert, N. P. Meredith, and R. R. Anderson (2005), Timescale for radiation belt electron acceleration by whistler mode chorus waves, *J. Geophys. Res.*, *110*, A03225, doi:10.1029/2004JA010811.

Kasahara, Y., Y. Miyoshi, Y. Omura, O. P. Verkhoglyadova, I. Nagano, I. Kimura, and B. T. Tsurutani (2009), Simultaneous satellite observations of VLF chorus, hot and relativistic electrons in a magnetic storm "recovery" phase, *Geophys. Res. Lett.*, *36*, L01106, doi:10.1029/2008GL036454.

LeDocq, M. J., D. A. Gurnett, and G. B. Hospodarsky (1998), Chorus source locations from VLF Poynting flux measurements with the Polar spacecraft, *Geophys. Res. Lett.*, *25*, 4063–4066.

Li, W., R. M. Thorne, V. Angelopoulos, J. Bortnik, C. M. Cully, B. Ni, O. LeContel, A. Roux, U. Auster, and W. Magnes (2009), Global distribution of whistler-mode chorus waves observed on the THEMIS spacecraft, *Geophys. Res. Lett.*, *36*, L09104, doi:10.1029/2009GL037595.

Menietti, J. D., O. Santolik, and P. C. Abaci (2009), Chorus observations by the Polar spacecraft near the mid-altitude cusp, *Planet. Space Sci.*, *57*, 1412–1418, doi:10.1016/j.pss.2009.07.003.

Meredith, N. P., R. B. Horne, and R. R. Anderson (2001), Substorm dependence of chorus amplitudes: Implications for the acceleration of electrons to relativistic energies, *J. Geophys. Res.*, *106*, 13,165–13,178.

Meredith, N. P., R. B. Horne, D. Summers, R. M. Thorne, R. H. A. Iles, D. Heynderickx, and R. R. Anderson (2002), Evidence for acceleration of outer zone electrons to relativistic energies by whistler mode chorus, *Ann. Geophys.*, *20*, 967–979.

Meredith, N. P., M. Cain, R. B. Horne, R. M. Thorne, D. Summers, and R. R. Anderson (2003a), Evidence for chorus-driven electron acceleration to relativistic energies from a survey of geomagnetically disturbed periods, *J. Geophys. Res.*, *108*(A6), 1248, doi:10.1029/2002JA009764.

Meredith, N. P., R. B. Horne, R. M. Thorne, and R. R. Anderson (2003b), Favored regions for chorus-driven electron acceleration to relativistic energies in the Earth's outer radiation belt, *Geophys. Res. Lett.*, *30*(16), 1871, doi:10.1029/2003GL017698.

Meredith, N. P., R. B. Horne, R. M. Thorne, and R. R. Anderson (2009), Survey of upper band chorus and ECH waves: Implications for the diffuse aurora, *J. Geophys. Res.*, *114*, A07218, doi:10.1029/2009JA014230.

Nagano, I., S. Yagitani, H. Kojima, and H. Matsumoto (1996), Analysis of wave normal and Poynting vectors of the chorus emissions observed by GEOTAIL, *J. Geomagn. Geoelectr.*, *48*, 299–307.

Newman, M. (2005), Power laws, Pareto distributions and Zipf's law, *Contemp. Phys.*, *46*, 323–351, doi:10.1080/00107510500052444.

Omura, Y., N. Furuya, and D. Summers (2007), Relativistic turning acceleration of resonant electrons by coherent whistler mode waves in a dipole

magnetic field, *J. Geophys. Res.*, *112*, A06236, doi:10.1029/2006JA012243.

Omura, Y., Y. Katoh, and D. Summers (2008), Theory and simulation of the generation of whistler-mode chorus, *J. Geophys. Res.*, *113*, A04223, doi:10.1029/2007JA012622.

Parrot, M., O. Santolík, N. Cornilleau-Wehrlin, M. Maksimovic, and C. Harvey (2003a), Source location of chorus emissions observed by Cluster, *Ann. Geophys.*, *21*, 473–480.

Parrot, M., O. Santolík, N. Cornilleau-Wehrlin, M. Maksimovic, and C. Harvey (2003b), Magnetospherically reflected chorus waves revealed by ray tracing with Cluster data, *Ann. Geophys.*, *21*, 1111–1120.

Parrot, M., O. Santolík, D. Gurnett, J. Pickett, and N. Cornilleau-Wehrlin (2004), Characteristics of magnetospherically reflected chorus waves observed by Cluster, *Ann. Geophys.*, *22*, 2597–2606.

Pokhotelov, D., F. Lefeuvre, R. B. Horne, and N. Cornilleau-Wehrlin (2008), Survey of ELF-VLF plasma waves in outer radiation belt observed by Cluster STAFF-SA experiment, *Ann. Geophys.*, *26*, 3269–3277.

Pope, J. H. (1963), A high-latitude investigation of the natural very-low-frequency electromagnetic radiation known as chorus, *J. Geophys. Res.*, *68*, 83–99, doi:10.1029/JZ068i001p00083.

Roederer, J. G. (1970), *Dynamics of Geomagnetically Trapped Radiation*, Springer, Berlin.

Santolík, O. (2008), New results of investigations of whistler-mode chorus emissions, *Nonlinear Processes Geophys.*, *15*, 621–630.

Santolík, O., and J. Chum (2009), The origin of plasmaspheric hiss, *Science*, *324*, 729–730, doi:10.1126/science.1172878.

Santolík, O., and M. Parrot (2000), Application of wave distribution function methods to an ELF hiss event at high latitudes, *J. Geophys. Res.*, *105*, 18,885–18,894.

Santolík, O., J. S. Pickett, D. A. Gurnett, and L. R. O. Storey (2002), Magnetic component of narrowband ion cyclotron waves in the auroral zone, *J. Geophys. Res.*, *107*(A12), 1444, doi:10.1029/2001JA000146.

Santolík, O., D. A. Gurnett, J. S. Pickett, M. Parrot, and N. Cornilleau-Wehrlin (2003a), Spatio-temporal structure of storm-time chorus, *J. Geophys. Res.*, *108*(A7), 1278, doi:10.1029/2002JA009791.

Santolík, O., M. Parrot, and F. Lefeuvre (2003b), Singular value decomposition methods for wave propagation analysis, *Radio Sci.*, *38*(1), 1010, doi:10.1029/2000RS002523.

Santolík, O., E. Macúšová, K. H. Yearby, N. Cornilleau-Wehrlin, and H. S. K. Alleyne (2005), Radial variation of whistler-mode chorus: First results from the STAFF/DWP instrument onboard the Double Star TC-1 spacecraft, *Ann. Geophys.*, *23*, 2937–2942.

Santolík, O., J. Chum, M. Parrot, D. A. Gurnett, J. S. Pickett, and N. Cornilleau-Wehrlin (2006), Propagation of whistler mode chorus to low altitudes: Spacecraft observations of structured ELF hiss, *J. Geophys. Res.*, *111*, A10208, doi:10.1029/2005JA011462.

Shprits, Y. Y., N. P. Meredith, and R. M. Thorne (2007), Parameterization of radiation belt electron loss timescales due to interactions with chorus waves, *Geophys. Res. Lett.*, *34*, L11110, doi:10.1029/2006GL029050.

Sigsbee, K., J. D. Menietti, O. Santolík, and J. S. Pickett (2010), Locations of chorus emissions observed by the Polar Plasma Wave Instrument, *J. Geophys. Res.*, *115*, A00F12, doi:10.1029/2009JA014579.

Storey, L. R. O. (1953), An investigation of whistling atmospherics, *Philos. Trans. R. Soc. London, Ser. A*, *246*, 113–141.

Summers, D., B. Ni, and N. P. Meredith (2007), Timescales for radiation belt electron acceleration and loss due to resonant wave-particle interactions: 2. Evaluation for VLF chorus, ELF hiss, and electromagnetic ion cyclotron waves, *J. Geophys. Res.*, *112*, A04207, doi:10.1029/2006JA011993.

Trakhtengerts, V. Y., A. G. Demekhov, E. E. Titova, B. V. Kozelov, O. Santolik, E. Macusova, D. Gurnett, J. S. Pickett, M. J. Rycroft, and D. Nunn (2007), Formation of VLF chorus frequency spectrum: Cluster data and comparison with the backward wave oscillator model, *Geophys. Res. Lett.*, *34*, L02104, doi:10.1029/2006GL027953.

Tsurutani, B. T., and E. J. Smith (1974), Postmidnight chorus: A substorm phenomenon, *J. Geophys. Res.*, *79*, 118–127.

Tsurutani, B. T., and E. J. Smith (1977), Two types of magnetospheric ELF chorus and their substorm dependence, *J. Geophys. Res.*, *82*, 5112–5128.

Tsurutani, B. T., et al. (2006), Corotating solar wind streams and recurrent geomagnetic activity: A review, *J. Geophys. Res.*, *111*, A07S01, doi:10.1029/2005JA011273.

Tsurutani, B. T., O. P. Verkhoglyadova, G. S. Lakhina, and S. Yagitani (2009), Properties of dayside outer zone chorus during HILDCAA events: Loss of energetic electrons, *J. Geophys. Res.*, *114*, A03207, doi:10.1029/2008JA013353.

Tsyganenko, N. A. (1989), A magnetospheric magnetic field model with a warped tail current sheet, *Planet. Space Sci.*, *37*, 5–20, doi:10.1016/0032-0633(89)90066-4.

Tsyganenko, N. A. (1995), Modeling the Earth's magnetospheric magnetic field confined within a realistic magnetopause, *J. Geophys. Res.*, *100*, 5599–5612, doi:10.1029/94JA03193.

Tsyganenko, N. A., and M. I. Sitnov (2005), Modeling the dynamics of the inner magnetosphere during strong geomagnetic storms, *J. Geophys. Res.*, *110*, A03208, doi:10.1029/2004JA010798.

Vaivads, A., O. Santolík, G. Stenberg, M. André, C. J. Owen, P. Canu, and M. Dunlop (2007), Source of whistler emissions at the dayside magnetopause, *Geophys. Res. Lett.*, *34*, L09106, doi:10.1029/2006GL029195.

Verkhoglyadova, O. P., B. T. Tsurutani, Y. Omura, and S. Yagitani (2009), Properties of dayside nonlinear rising tone chorus emissions at large L observed by GEOTAIL, *Earth Planets Space*, *61*, 625–628.

D. A. Gurnett, J. D. Menietti, and J. S. Pickett, Department of Physics and Astronomy, University of Iowa, Iowa City, IA 52242-1479, USA. (donald-gurnett@uiowa.edu; john-menietti@uiowa.edu; pickett@uiowa.edu)

O. Santolík, Institute of Atmospheric Physics, Boční II 1401, 141 31 Praha 4, Czech Republic. (ondrej.santolik@mff.cuni.cz)

B. T. Tsurutani and O. Verkhoglyadova, Jet Propulsion Laboratory, 4800 Oak Grove Dr., Pasadena, CA 91109, USA. (bruce.t.tsurutani@jpl.nasa.gov; olga.verkhoglyadova@jpl.nasa.gov)